Multiple-Bandgap Photoelectrochemistry: Bipolar Semiconductor Ohmic Regenerative Electrochemistry

S. Licht,* O. Khaselev, and P. A. Ramakrishnan

Department of Chemistry, Technion−Israel Institute of Technology, Haifa, 32000, Israel

T. Soga and M. Umeno

Nagoya Institute of Technology, Gokiso-Cho, Showa-ku, Nagoya 466, Japan

Received: November 2, 1997

Multiple semiconductor bandgaps can enhance the energetics of photoelectrochemical interactions. However, illuminated bipolar multiple bandgaps can generate a photopotential larger than the thermodynamic electrochemical potential window of many solvents and induce parasitic chemical reactions including solvent decomposition and electrode deactivation, which could inhibit regenerative photoelectrochemistry. From a fundamental and experimental perspective, it is demonstrated that these parasitic reactions may be avoided and that several efficient regenerative bipolar bandgap photoelectrochemical processes can occur. A bipolar ohmic regenerative photoelectrochemical cell contains wide bandgap pn junctions in tandem monolithic contact with smaller bandgap pn junctions. The small-bandgap semiconductor is either in direct ohmic contact with a regenerative solution-phase redox couple or in indirect contact through an electrocatalyst intermediate. The photocathodic bipolar ohmic regenerative chemistry is given by $h\nu \Rightarrow$ pn (wide gap)|pn (small gap)|(redox couple)|(electrocatalyst anode). Energy diagrams of photocathodic bipolar ohmic regenerative photoelectrochemistry are evaluated and studied with several AlGaAs|Si|electrolyte photoelectrochemical cells. The individual multiple-bandgap components include a graded band emitter, varying from $Al_{(0.3−0.15)}Ga_{(0.7−0.85)}As$, and a Si layer either in direct contact with a $V^{2+/3+}$ electrolyte or in indirect contact with a $V^{2+/3+}$, polysulfide, or iodide aqueous electrolyte through a carbon, CoS, or Pt electrocatalyst, respectively. The electrocatalyst prevents any electrolyte-induced semiconductor photocorrosion. Under solar illumination, photopotentials larger than the 1.2-V solvent-decomposition potential are generated (open circuit potentials from 1.4 to 1.5 V), and efficient regenerative photoelectrochemistry occurs at 19%−20% solar energy conversion efficiency.

Introduction

Photoelectrochemical energy conversion consists of a hybrid encompassing electrochemistry, spectroscopy, and solid-state physics. Important early fundamental studies on the electrochemistry of illuminated immersed semiconductors[1,2] led to the simultaneous demonstration in 1976 by groups at Bell Labs, the Weizmann Institute of Science, and MIT of regenerative photoelectrochemical solar cells (PECs).[3−5] In these cells the solution-phase species, which was oxidized at the n-type semiconductor surface, was then reduced (regenerated) at an appropriate electrocatalytic second electrode.

With few exceptions, photoelectrochemical systems are susceptible to photoinduced corrosion of the semiconductor surface, which can suppress constructive photodriven redox processes within minutes of irradiation.[6] Semiconductor surface modification, and in particular photoetching, increases microscopic surface morphology at the semiconductor−electrolyte interface and significantly suppresses photocorrosion.[7] Changes in solution-phase chemistry can enhance photoelectrochemical solar-to-electrical energy conversion and impede photocorrosion.[8] Electrolyte modification inhibited thin-film n-Cd (Se,-Te) photocorrosion, supporting continuous polysulfide redox chemistry for a lifetime of 1 year, consistent with a chemical description of photoelectrochemical energy conversion.[9] Recently, new insights to understanding charge-transfer kinetics

in photoelectrochemical systems[10] have been facilitated by techniques such as microwave photoelectrochemical spectroscopy.[11]

From a fundamental perspective, the use of multiple-bandgap devices can lead to the more efficient matching and utilization of the solar spectra.[12−16] Solid-state multiple-bandgap usage has also been referred to as a photovoltaic tandem, multiple-window, split-spectrum, or cascade structure in various studies.[13,14] Two or more bandgap configurations will lead, per unit surface area, to more efficient solar-energy conversion, and in the solid state, multiple-bandgap solar cells have already achieved more than 30% conversion efficiency of solar-to-electrical energy for both one sun and for concentrated-sun insolation.[15] Present solid-state (photovoltaic) multijunction photovoltaics exist in one of two modes, either splitting (in which the solar spectrum is optically separated prior to incidence on the cells) or stacked devices. The latter mode has been developed as either monolithic (integrated) or mechanically (discrete cells layered with transparent adhesive) stacked cells. Most monolithic-stacked multijunction photovoltaics under development use III−V semiconductors in at least one of the layers and take advantage of the variations in bandgap and close lattice match achieved with other related III−V alloys. For example, GaInP has been used as a wide-gap top cell, or GaSb
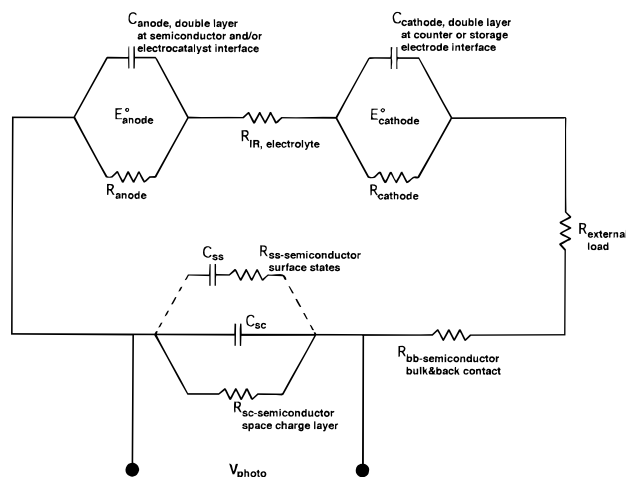
Bipolar Semiconductor Electrochemistry

J. Phys. Chem. B, Vol. 102, No. 14, 1998 **2537**

Figure 1. Equivalent circuit representation of a cell containing an illuminated semiconductor electrode and a counter electrode immersed in solution. The photopotential E_{photo} can generate current through an external load $R_{external}$.

and GaInAsP as small-gap lower cells, for III−V top-layer multijunction cells; other cells use silicon or CIS cells as a lower layer.[13−16]

When photoelectrochemical cells were first introduced, extensive descriptions of the energy-conversion mechanism in solid-state solar cells, such as the conventional silicon photovoltaic solar cell, were already available.[17,18] In addition, there are several mechanistic components exclusive to the photoelectrochemical environment. A variety of models have been used to represent an equivalent circuit for photoelectrochemical charge transfer. Significant components of several such schemes are presented in Figure 1 for a photoanodic process.[19−23] The components permit charge transfer (i) from the semiconductor space-charge layer and/or the surface states or (ii) directly into the solution and/or through an electrocatalyst into the solution (iii) through the bulk electrolyte (iv) into the cathodic counter electrode or storage-electrode process and (v) external load, and finally, (vi) through the semiconductor bulk via a back contact. Similarly, a photocathodic process contains a photocathode and a counter anode. Under illumination, an anodic or cathodic photopotential V_{photo} driving a photocurrent J_{ph} is segmented into a potential drop over the external load, over the bulk electrolyte and semiconductor, and over polarization η_{anode} and $\eta_{cathode}$ in anodic and cathodic processes:

$$V_{photo} = J_{ph}(R_{load} + R_{IR} + R_{bb}) + (E^{\circ}_{anode} + \eta_{anode}) - (E^{\circ}_{cathode} + \eta_{cathode}) \quad (1)$$

Potential losses in the bulk electrolyte, bulk semiconductor, and back contact are minimized through electrolytic and solid-state control, simplifying eq 1 to

$$V_{photo} = J_{ph}R_{load} + (E^{\circ}_{anode} + \eta_{anode}) - (E^{\circ}_{cathode} + \eta_{cathode}) \quad (2)$$

Multiple-bandgap photoelectrochemical cells (MPECs) may generate substantially larger photopotentials than conventional PECs. Independent of the equivalent circuit used to model a PEC, two cases of limiting potential are relevant to optimizing MPECs. The majority of the V_{photo} drop occurs (a) over an external load or alternatively (b) over the electrodes in solution. These two cases are illustrated through use of Figure 1. (a) In a regenerative PEC, used to maximize power through $R_{external}$ in Figure 1, $E^{\circ}_{anode} = E^{\circ}_{cathode}$. With effective electrocatalysis

in a conductive electrolyte, potential losses, primarily as cathodic and anodic overpotential, are small. Hence, in a regenerative PEC, V_{photo} generally will not induce electrolysis. The majority of V_{photo} is expressed as an IR drop over R_{load}, and even a MPEC large photopotential can be sustained at

$$V_{photo} = J_{ph}R_{load} + (\eta_{anode} - \eta_{cathode}) \quad (3)$$

(b) In a storage PEC, $E^{\circ}_{anode} \neq E^{\circ}_{cathode}$, the potential drop occurs primarily over the immersed electrodes. Storage can consist of both in situ or electrolysis cells. Solvent decomposition may be the desired end product, as in the case of photoelectrolysis to generate H_2 and O_2. In this case, a large photopotential may be attractive. However, solvent breakdown generally represents a parasitic reaction that will both diminish storage efficiency and decompose the cell. A large MPEC V_{photo} can induce solution electrolysis. In this developing series of papers, several physical and chemical means will be probed to overcome this obstacle.

Potential benefits of multiple-band semiconductors for the electrolysis of water and photoelectrochemistry have been discussed as early as 1975[24−26] and provide impetus for the study of multiple-bandgap photoelectrochemistry. Several specific energetic semiconductor and electrolyte interactions are of particular importance to multiple-bandgap photoelectrochemistry. Although not elucidated in these early studies, successive solid-state multiple bandgaps may be arranged in either a bipolar (for example, a pn−pn) order or an inverted (for example, a pn−np) order. Both inverted or bipolar multiple bandgaps can utilize either a Schottky or ohmic photoelectrochemical solution interface, and each can be either regenerative, generating external electrical work in which no net change in electrolyte composition occurs, or a storage cell in which separate redox reactions are driven.

In this study, the chemistry and physics of bipolar bandgap ohmic photoelectrochemistry is explored. It is demonstrated that the energetic photopotentials of such multiple-bandgap systems need not facilitate parasitic solvent decomposition and that efficient stabilized charge transfer can occur in multiple-bandgap photoelectrochemical systems. Incident photons can be localized for electron/hole-pair charge generation within the multiple-bandgap semiconductor small and wide bandgap regions rather than lost through competitive electrolyte light absorption. An electrocatalyst intermediate inhibits any electrolyte-induced semiconductor photocorrosion. Combined, these effects can lead to higher multiple-bandgap photoelectrochemical solar-to-electrical conversion efficiency than previously observed in single-gap photoelectrochemistry.

Experimental Section

Materials. *Preparation of Electrolytes.* Analytical-grade reagents and distilled, doubly deionized water were used throughout and were prepared, stored, and utilized under argon to prevent reaction with oxygen. The V(II)−V(III) redox couple solution was prepared by reducing V_2O_5 with a small excess of Zn-metal powder (corresponding to the stoichiometry for V(V) to V(II)) in aqueous HCl electrolyte to yield 4 M HCl after the reaction. The total amount of vanadium in the solution is 0.35 M. The solution potential was measured to be −0.45 V versus Ag/AgCl reference. The electrolyte containing the iodide redox couple was prepared by addition of iodine (I_2) to concentrated aqueous HI. Preparation of the polysulfide redox couple was prepared via synthesis of KHS. KHS solutions were prepared by saturation of KOH solutions with H_2S_{gas}. The reaction is

exothermic and results in an increase in volume, a proportional mass increase, and a pH decrease all consistent with the equation

$$KOH + H_2S \rightarrow KHS + H_2O \qquad (4)$$
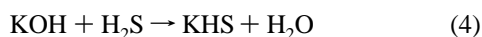
As measured by proportional mass increase, the KHS solution synthesis proceeds to $99.3 \pm 0.6\%$ completion. Polysulfide solutions are then formed by addition of KOH and sulfur to these KHS solutions. Concentrated KOH, KHS, and polysulfide solutions were stored in polypropylene vessels.

Preparation of Electrodes and Multiple-Gap Cells. The preparation of AlGaAs/Si bipolar and GaAs/Si solid-state components is by epitaxial growth performed using conventional atmospheric-pressure metal organic chemical vapor deposition (MOCVD). Trimethyl gallium, trimethyl aluminum, diethyl zinc, AsH$_3$, and H$_2$Se are used as the source materials for Ga, Al, Zn, As, and Se, respectively. The effects of the growth sequence and a graded band emitter layer are as previously described.[16,27−30] The Si substrate is a Czochralski (Cz) grown single crystal with the orientation of [100], 2° off toward [011]. GaAs is grown on Si by a two-step growth method with 10-nm-thick GaAs buffer layer grown at 400 °C. AlGaAs layers and a p-GaAs cap layer are grown on Si sequentially. Antireflection films are of MgF$_2$/ZnS double layers. Au−Zn/Au is evaporated as the electrical contact for p-type electrodes. The lower n$^+$-Si overlayer is exposed to the solution or Au−Sb/Au is evaporated as an electrical contact, followed by an electrocatalytic Pt or CoS layer for either the iodide or sulfide electrolytes. CoS was formed by electrodeposition of Co at 50 mA/cm^2 from a 50 °C 2 *m* CoSO$_4$, 0.6 *m* boric acid, 0.2 *m* NaCl solution onto a 25-μm brass substrate followed by oxidation in polysulfide solution as previously described.[31]

Instrumentation and Measurement Techniques. Outdoor photoelectrochemical measurements of solar-cell efficiency were redundantly measured both with a simple resistive load and also with a potential-controlled PINE AFCBP1 bipotentiostat (using a conventional two-electrode cell configuration), and the cell photocurrent was monitored using National Instruments analog/digital data acquisition. Insolation was measured by the Israel Meteorological Society. Indoor photocurrent stability and (dark) polarization measurements were conducted in a three-electrode cell with the Pine bipotentiostat a large Pt-mesh counter electrode and a Pt reference. Indoor illumination was provided by a 20-W tungsten−halogen lamp.

Results and Discussion

Several physical chemical challenges that impede effective multiple-bandgap photoelectrochemistry exist. A large MPEC V_{photo} can generate a photopotential larger than the thermodynamic electrochemical potential window of many solvents. Solution-phase modification can expand the sustainable electrolyte potential window, preventing the onset of solvent decomposition (electrolysis). As shown in Table 1 for iodide electrolytes, replacement of HI by KI decreases the magnitude of electrolytic hydrogen evolution by increasing the proportion of charge transfer as regenerative iodide redox chemistry. Similarly, a 40-fold increase in iodine concentration increases active redox reduction and also expands the accessible potential window. As summarized in Table 1, potentials substantially larger than the 1.2-V water-decomposition potential are readily sustained without H$_2$ or O$_2$ evolution.

Other high-photopotential challenges include electrocatalytic activity loss. Exemplified in Table 2 is the high-overpotential losses of the polysulfide electrocatalytic CoS counter electrode,

TABLE 1: Competition between Regenerative Iodide Redox Chemistry and Water Electrolysis at Various Applied Potentials and in Several Electrolytes

electrolyte/electrodes	$E_{applied}$ (V)	$E_{cathode}$ vs AgCl (V)	Q^a for H$_2$ (%)	Q^a for O$_2$ (%)
10.4 M HI, 0.01 M I$_2$/Ni	0.0	+0.2	0	0
10.4 M HI, 0.01 M I$_2$/Ni	1.0	−0.7	12	0
3 M KI, 0.01 M I$_2$/Ni	0.0	+0.2	0	0
3 M KI, 0.01 M I$_2$/Ni	1.0	−0.7	0	0
3 M KI, 0.01 M I$_2$/Ni	2.0	−1.3	33	0
3 M KI, 0.1 M I$_2$/Ni	0.0	+0.3	0	0
3 M KI, 0.1 M I$_2$/Ni	1.0	−0.6	0	0
3 M KI, 0.1 M I$_2$/Ni	2.0	−1.3	9.4	0
3 M KI, 0.4 M I$_2$/Ni	0.0	+0.3	0	0
3 M KI, 0.4 M I$_2$/Ni	1.0	−0.1	0	0
3 M KI, 0.4 M I$_2$/Ni	2.0	−0.7	0	0
3 M KI, 0.4 M I$_2$/Ni	2.5	−1.1	0	0

^{a} Q is the proportion of the measured current that generates the indicated gas, rather than driving the I$^-$/I$_3^-$ redox couple.

TABLE 2: Loss at High Applied Potentials of Polysulfide Electrocatalytic Activity at a Cobalt Sulfide Electrode^a

electrolyte/electrodes	$E_{applied}$ (V)	$E_{cathode}$ vs AgCl (V)	Q for H$_2$ or O$_2$ (%)	η_{total} (mV cm^2 mA^{-1})
1 M Na$_2$S$_2$, 1 M NaOH/CoS	0.0	−0.7	0	
1 M Na$_2$S$_2$, 1 M NaOH/CoS	0.5	−1.0	0	2
1 M Na$_2$S$_2$, 1 M NaOH/CoS	1.0	−1.2	0	2
1 M Na$_2$S$_2$, 1 M NaOH/CoS	2.0	−1.3	0	19

^{a} η_{total} is the measured polarization loss, and Q is the proportion of the measured current that generates the indicated gas.

which will occur at high negative bias, due to CoS reduction to cobalt metal. These losses will diminish the fill factor and lead to losses in solar-cell conversion efficiencies. However, as described by eq 3, in a regenerative as opposed to a storage PEC, the majority of V_{photo} is expressed as an IR drop over R_{load}. In this case of a regenerative photoelectrochemical solar cell (PEC), V_{photo} generally will not induce electrolysis or electrocatalyst decomposition. The majority of V_{photo} is expressed as an IR drop over R_{load}. Hence, even a large multiple-bandgap photoelectrochemical solar cell (MPEC) photopotential can be sustained.

This study probes several of the physical chemical challenges impeding effective multiple-bandgap photoelectrochemistry through the conceptually simplest multiple-bandgap photoelectrochemical system (more complex systems are being studied in subsequent papers). A bipolar-gap *direct-ohmic* photoelectrochemical system comprises either a bipolar-bandgap pnpn|electrolyte ohmic photoelectrochemical cell, with reduction occurring at the photoelectrode/electrolyte interface and regenerative oxidation occurring at the electrolyte/counter electrode (anode) interface, or alternatively, an npnp|electrolyte bipolar bandgap with oxidation occurring at the semiconductor/electrolyte interface and regenerative reduction occurring at the electrolyte/counter electrode interface. In the bipolar-gap *direct-ohmic* photoelectrochemical system, *direct* refers to the direct contact between semiconductor and solution and *ohmic* indicates this interface is an ohmic rather than a Schottky junction. This facilitates study of several characteristics of bipolar multiple-bandgap systems without the added complication of simultaneous parametrization of a direct Schottky barrier at the electrolyte interface.

Relevant parameters to the bipolar-gap direct-ohmic photoelectrochemical system include the quasi Fermi level under illumination, E_{Fermi}, in layers that may be p-type or n-type and comprised of "w" wide-bandgap or "s" smaller-bandgap semiconductors. E_G, E_{VB}, and E_{CB} express the bandgap and valence

Bipolar Semiconductor Electrochemistry

J. Phys. Chem. B, Vol. 102, No. 14, 1998 **2539**

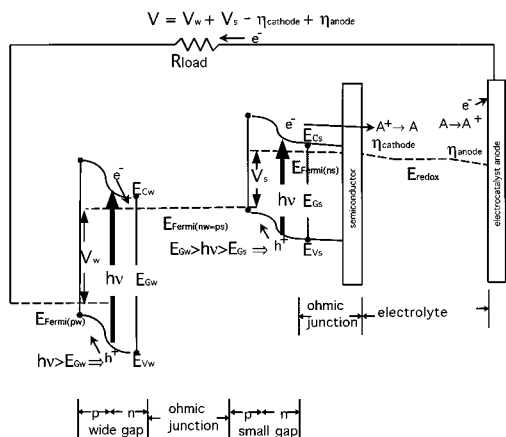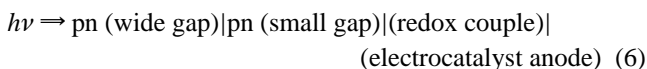$$V = V_{\text{w}} + V_{\text{s}} - \eta_{\text{cathode}} + \eta_{\text{anode}}$$

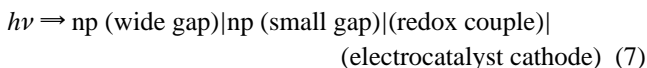**Figure 2.** Energy diagram for bipolar direct-ohmic multijunction regenerative photoelectrochemistry.

and conduction bands of various semiconductor layers in these systems. Under illumination, an anodic or cathodic photopotential V_{photo} drives a photocurrent J_{ph}. The photopotential is segmented into a potential drop over an external load R_{load}, the resistance of the bulk electrolyte R_{IR} and semiconductor R_{bb}, and the polarization η_{anode} and η_{cathode} in the regenerative anodic and cathodic processes. The simplest MPEC contains two adjacent bandgaps. As shown in the photocathodic energy diagram of a bipolar regenerative MPEC in Figure 2, the generated photovoltage V_{photo} is the sum of the potentials generated through individual wide- and small-bandgap layers minus cathodic and anodic polarization losses in driving a regenerative redox couple:

$$V_{\text{photo}} = V_{\text{w}} + V_{\text{s}} - \eta_{\text{cathode}} + \eta_{\text{anode}} \qquad (5)$$

This description, eq 5, is consistent with either a photocathodic-driven regenerative solution-phase redox couple

$$h\nu \Rightarrow \text{pn (wide gap)}|\text{pn (small gap)}|(\text{redox couple})|$$
$$(\text{electrocatalyst anode}) \quad (6)$$

or a photoanodic-driven redox couple

$$h\nu \Rightarrow \text{np (wide gap)}|\text{np (small gap)}|(\text{redox couple})|$$
$$(\text{electrocatalyst cathode}) \quad (7)$$

The PEC requires an accessible ohmic solid/semiconductor interface to permit application of an external cell load, and also internal solid/electrolyte interfaces to facilitate ionic charge transfer. As shown in Figure 2, the photocathodic bipolar direct-ohmic MPEC comprises a two-photon/one-electron photoelectrochemical process ($2h\nu \rightarrow \text{e}^-$), which may be generalized for a system consisting of n different bandgap layers to an n-photon process ($nh\nu \rightarrow \text{e}^-$). Light shown incident from the left side of the energy scheme first enters the wide-bandgap layer(s) in which more energetic photons are absorbed; less energetic photons are transmitted through this upper layer and are absorbed by the small-bandgap layer. The resultant combined potential of the photodriven charge sustains reduction at the photocathode interface and drives extractable work through the external load R_{load}.

In Figure 2, light of energy greater than the bandgap energy E_{Gw} drives electron/hole-pair excitation:

$$\text{h}^+\text{e}^- + h\nu \ (h\nu > E_{\text{Gw}}) \rightarrow \text{h}^+ + \text{e}^-* \qquad (8)$$
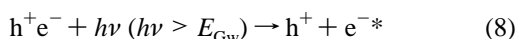
h^+ travels into the quasi Fermi level of the wide-gap p-type

layer. The pn space-charge layer inhibits charge recombination, driving the photoexcited electron e^-* from the (p-type) conduction to the (n-type) valence band. The photopotential of a single pn junction is[32]

$$V_{\text{pn}} = (nkT/e)\ln[1 + j_{\text{ph,pn}}/j_{\text{o,pn}}] \qquad (9)$$

where V_{pn} is constrained by the photocurrent density through the junction $j_{\text{ph,pn}}$. $j_{\text{o,pn}}$ is the saturation current (of a reversely polarized diode) and is described by the Shockley equation when the forward current is determined by injection and recombination of minority carriers. For a material of intrinsic carrier density n_{i}

$$j_{\text{o,pn}} = en_{\text{i}}^2\left[\frac{D_{\text{p}}}{N_{\text{D}}L_{\text{p}}} + \frac{D_{\text{n}}}{N_{\text{V}}L_n}\right] \qquad (10)$$

in which D_{n}, D_{p}, L_{n}, and L_{p} are the electron and hole diffusion constants and lengths, while N_{D} and N_{V} are the corresponding donor and acceptor densities. Continuing toward the right in this figure, charge excited by the wide-bandgap photon is neutralized at the small-bandgap layer, where further stimulation by longer-wavelength light occurs:

$$\text{h}^+\text{e}^-* + h\nu \ (h\nu > E_{\text{Gs}}) \rightarrow \text{h}^+ + \text{e}^-** \qquad (11)$$
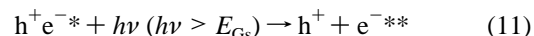
Charge recombination is inhibited by the small-bandgap pn junction, and drives the photoexcited electron e^-** from the n-type (small-bandgap) conduction band into the electrolyte, where solution-phase reduction occurs:

$$\text{A}^+ + \text{e}^- \rightarrow \text{A} \qquad (12)$$

Generated charge flows through all layers of the cell, providing the additional constraint

$$j_{\text{ph,pn}-\text{w}} = j_{\text{ph,pn}-\text{s}} \qquad (13)$$

The lowest semiconductor layer (the small-bandgap n-type layer in the figure) remains in direct contact with the electrolyte. As indicated, this contact is ohmic and is not the source of the (pn) space-charge field preventing recombination in the small-bandgap layers. Cell photovoltage through R_{load} is limited by the consecutive wide- and small-bandgap pn junctions, which yields from eqs 5 and 9

$$V_{\text{bipolar ohmic}} = (nkT/e)(\ln[1 + j_{\text{ph}}/j_{\text{o,pn}-\text{w}}][1 + j_{\text{ph}}/j_{\text{o,pn}-\text{s}}]) - \eta_{\text{cathode}} + \eta_{\text{anode}} \quad (14)$$

in which the photopower generated by a bipolar regenerative MPEC is given by the product

$$P_{\text{bipolar regenerative}} = j_{\text{ph}}[(nkT/e)(\ln[1 + j_{\text{ph}}/j_{\text{o,pn}-\text{w}}][1 + j_{\text{ph}}/j_{\text{o,pn}-\text{s}}]) - \eta_{\text{cathode}} + \eta_{\text{anode}}] \quad (15)$$

This study utilizes multijunction solid-state layers providing a bipolar AlGaAs ($E_{\text{Gw}} = 1.6$ eV) wide bandgap overlayed on a Si ($E_{\text{Gs}} = 1.0$ eV) small bandgap. Photovoltaic cells based on two-bandgap and/or graded-bandgap materials that are arranged in multiple-stacked monolithic junctions are under intensive development, and high solar-to-electrical conversion efficiencies ranging from 19% to 30% have been reported for several of these solid-state devices. Challenges include the complexity of multiple-junction formation and photocurrent matching of the various illuminated bandgap materials. The highest confirmed conversion efficiencies for multijunction
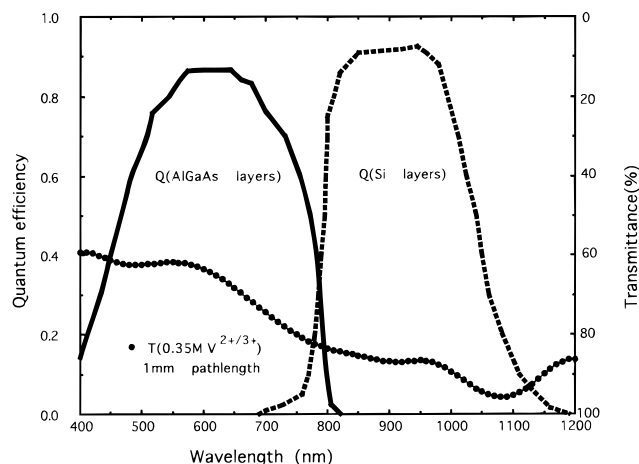
Figure 3. Overlay of the optical characteristics of the solid- and solution-phase of the AlGaAs/Si solid state and $V^{3+/2+}$ electrolyte constituents within a bipolar-gap photoelectrochemical cell. Transmission of the $V^{3+/2+}$ electrolyte is measured through a path length of 1 mm. The Si bottom cell consists of a p^+-Si, n-Si, and n^+-Si multijunction. As described in the text, the $Al_{(0.3-0.15)}Ga_{(0.7-0.85)}As$ top cell utilizes a graded band emitter, varying from $Al_{(0.3-0.15)}Ga_{(0.7-0.85)}As$, and the Si bottom cell consists of a p^+-Si, n-Si, and n^+-Si multijunction.

Figure 4. Schematic description of the components in the bipolar-gap direct-ohmic AlGaAs|Si|$V^{3+/2+}$ photoelectrochemical solar cell.

photovoltaics include at one sun 30.3% for a 4-cm^2 GaInP|GaAs monolithic cell by Japan Energy in 1996, 25.8% for a 4-cm^2 GaAs|CIS (thin film) cell by Kopin/Boeing in 1989,[15] and 20.6% for an AlGaAs|Si solar cell at the Nagoya Institute of Technology.[16] Despite the lower efficiencies, in principle, the Si bottom-layer cell provides advantages, both in cost, availability and high-production technologies of silicon, and in the near-ideal bandgap of 1.0 eV for a bottom-layer material.

Figure 3 overlays the optical characteristics of the solid and solution phase of the AlGaAs|Si solid-state and $V^{3+/2+}$-electrolyte-optimized components within a bipolar-gap photoelectrochemical cell. The aqueous vanadium electrolyte exhibits distinctive absorption throughout the visible and near-IR spectra. Three of the observed electrolyte transmission minima are due to solvated $V^{3+/2+}$ and occur at 400, 600, and 890 nm with the following: extinction coefficient $\epsilon(400 \text{ nm}) = 6.4 \text{ cm}^{-1} \text{ mol}^{-1}$, half-width $\Delta\lambda(400 \text{ nm}) = 100 \text{ nm}$; $\epsilon(600 \text{ nm}) = 4.5 \text{ cm}^{-1} \text{ mol}^{-1}$, $\Delta\lambda(600 \text{ nm}) = 150 \text{ nm}$; $\epsilon(890 \text{ nm}) = 0.8 \text{ cm}^{-1} \text{ mol}^{-1}$, $\Delta\lambda(890 \text{ nm}) = 120 \text{ nm}$. The remaining two of the observed transmission minima are due to solvent (H_2O and OH^-) absorbance and occur at 976 and 1200 nm with the following: extinction coefficient $\epsilon(976 \text{ nm}) = 0.24 \text{ cm}^{-1} \text{ mol}^{-1}$, half-width $\Delta\lambda(976 \text{ nm}) = 60 \text{ nm}$; $\epsilon(1200 \text{ nm}) = 0.60 \text{ cm}^{-1} \text{ mol}^{-1}$, $\Delta\lambda(1200 \text{ nm}) = 60 \text{ nm}$. Solution transmission is measured through a path length typical (1 mm) of many experimental front-wall photoelectrochemical cells. As is evident, light transmission interference will occur for the top AlGaAs layers and bottom Si layers through this or substantially shorter electrolyte path lengths. The solid-state component includes a graded band emitter varying from $Al_{(0.3-0.15)}Ga_{(0.7-0.85)}As$ with overlayers of p^+-$Al_xGa_{x-1}As$ on n-$Al_xGa_{x-1}As$. The effects of growth sequence and a graded band emitter layer on the improvement of collection efficiency have been previously described.[16,27-30] The Si bottom cell consists of a p^+-Si ($p = 1 \times 10^{19} \text{ cm}^{-3}$), n-Si ($n = 8 \times 10^{15} \text{ cm}^{-3}$), and n^+-Si ($n = 4 \times 10^{19} \text{ cm}^{-3}$) multijunction. The band edges observed in the figure at approximately 800 and 1100 nm are consistent with the respective AlGaAs and Si bandgaps.

For efficient electron/hole-pair charge generation, incident photons need to be localized within the multiple-bandgap semiconductor small- and wide-bandgap regions rather than lost
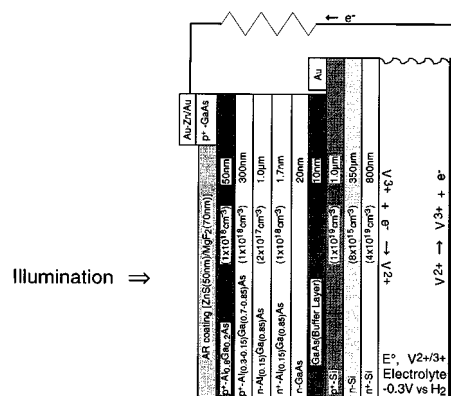
through competitive electrolyte light absorption. As seen in Figure 3, the vanadium electrolyte can significantly block light, over a wide range of visible and near-infrared wavelengths, from entering the wide- and small-bandgap layers of the multiple-bandgap photoelectrochemical cell. This deleterious effect is prevented by use of the back-wall multiple-bandgap photoelectrochemical cell presented in Figure 4. Light does not pass through the solution. As shown, illumination enters directly through antireflection films of 50-nm ZnS situated on 70-nm MgF$_2$. An evaporated Au−Zn|Au grid provides electrical contact to the wide-gap AlGaAs layers through a bridging p^+ = GaAs layer. Internally, a bridging GaAs buffer layer provides an ohmic contact between the wide-bandgap AlGaAs junctions and the lower Si layers. An intermediate contact layer indicated as "Au" is used only for probing separated characteristics of the wide- and small-bandgap junctions and is not utilized in the complete cell. Photogenerated charge at the indicated silicon−electrolyte interface induces solution-phase vanadium reduction in accord with

$$V^{3+} (+ h\nu) \rightarrow V^{2+} + h^+ \qquad (16)$$
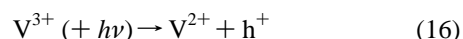
A carbon counter electrode provides an effective (low-polarization) electrocatalytic surface for the reverse process in a regenerative cell:

$$V^{2+} \rightarrow V^{3+} + e^- \qquad (17)$$

Additional constraints are imposed on multiple-bandgap photoelectrochemical solar cells compared to analogous photovoltaic devices. In single-bandgap photoelectrochemical solar cells, we have probed the manifold conditions in which solution-phase chemistry constrains the kinetics and thermodynamics of photoelectrochemical charge transfer. It has been previously demonstrated that modification of the solution-phase chemistry can substantially affect photoelectrochemical properties by (i) enhancing facile charge transfer, (ii) suppressing competing reactions, and suppressing both (iii) electrode and (iv) electrolyte decomposition products, as well as (v) substantially affecting the open-circuit photovoltage. These limitations have been studied in a variety of redox couples and electrolytes.[8,9] Solution-phase optimization is also critical to optimal performance of multiple-bandgap photoelectrochemical solar cells.

Heller, Miller et al., have previously shown that the p-Si surface is capable of sustaining minority-carrier injection into the solution and stabilizes reduction of the $V^{3+/2+}$ redox couple.[33] However, at n-Si this does not appear to be the case for reduction of the $V^{3+/2+}$ redox couple by majority-carrier injection into the solution. Thermodynamically, silicon can be
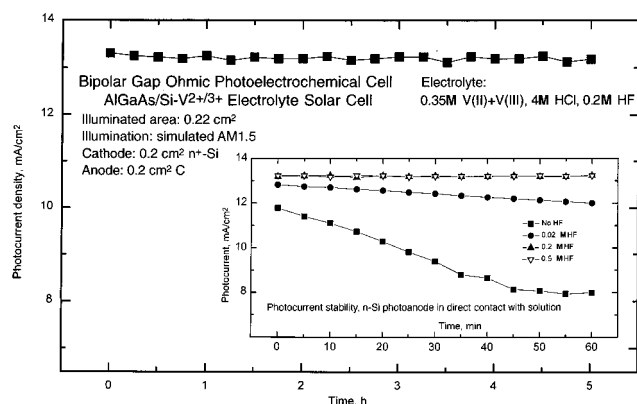
Bipolar Semiconductor Electrochemistry

J. Phys. Chem. B, Vol. 102, No. 14, 1998 **2541**

Figure 5. Photocurrent stability in several $V^{3+/2+}$ aqueous electrolytes of the bipolar-bandgap direct-ohmic AlGaAs|Si$-V^{3+/2+}$ photoelectrochemical cell (measured indoors using a tungsten halogen lamp to simulate outdoor AM1.5 insolation).
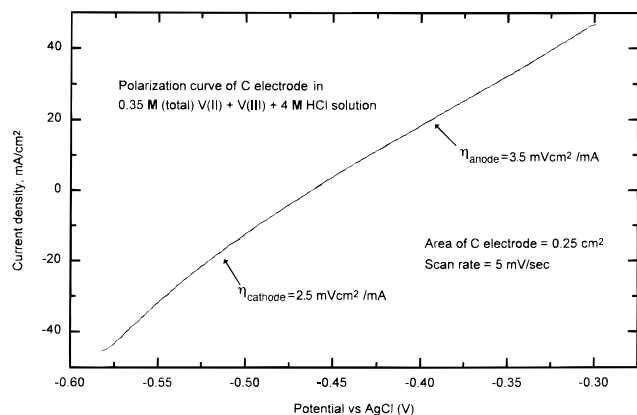

Figure 6. Current density for $V^{3+/2+}$ oxidation/reduction (in the dark) at carbon electrodes for various potentiostatic applied potentials at a linear sweep rate of 5 mV/s.

spontaneously oxidized in aqueous solution. This process may occur despite the photoinduced generation of reductive charge at the semiconductor/electrolyte interface. This is observed as the time-dependent decrease of the photocurrent under constant illumination during the photoinduced reduction of V^{2+} (by majority-carrier injection at n-Si) indicated in the inset Figure 5. This is consistent with the onset of surface passivation forming a layer that is passive to charge transfer and diminishes the photocurrent. The addition of a low concentration of HF to the electrolyte can remove this passivating layer and permit sustained photocurrent. This is illustrated in the inset of Figure 5 in which the addition of 0.02 and 0.2 M HF improves the photocurrent stability of this bipolar direct-ohmic MPEC. Also as shown, no further improvement in the photocurrent stability is observed when the HF concentration is further increased from 0.2 to 0.5 M HF. As presented in the main portion of Figure 5, the 0.2 M HF modified electrolyte stablizes the photocurrent at the n-Si interface for the measured period of several hours. As will be subsequently shown, photocurrent stability is further improved through use of an electrode catalyst bridging the silicon−electrolyte interface.

In accord with eq 15, maximization of the photopower necessitates minimization of the anodic and cathodic polarization losses η_{anode} and $\eta_{cathode}$ during charge transfer through the photoelectrode and counter electrode interfaces. Figure 6 presents the anodic and cathodic polarization curves for charge transfer to the $V^{3+/2+}$ redox couple through an effective electrocatalyst for this redox process (consisting of a carbon electrode). In the current domain investigated, polarization
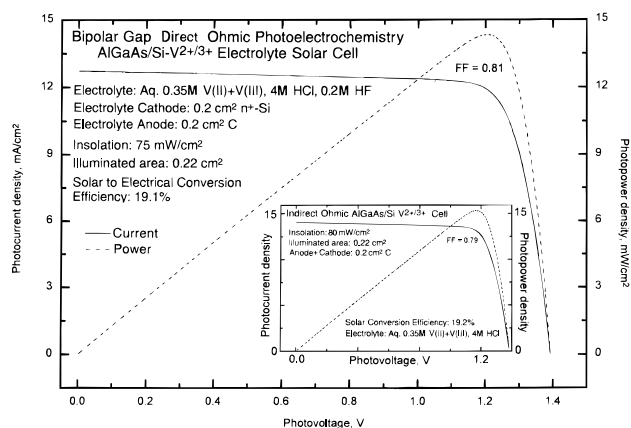

Figure 7. Measured outdoor photocurrent/voltage characteristics of the bipolar-gap *direct*-ohmic AlGaAs|Si|$V^{3+/2+}$ photoelectrochemical solar cell. Insolation was measured by the Israel Meteorological Society. The inset shows the measured outdoor photocurrent/voltage characteristics of the bipolar-gap *indirect*-ohmic AlGaAs|Si|$V^{3+/2+}$ photoelectrochemical solar cell.

losses are highly linear for both anodic and cathodic processes at 2.5−3.5 mV cm^2/mA and can create small but significant losses on the order of 10−100 mV in the MPEC.

Figure 7 presents the outdoor characteristics of the bipolar direct-ohmic AlGaAs|Si|$V^{2+/3+}$ photoelectrochemical cell under solar illumination. The system comprises the individual components illustrated in Figure 4 and uses an HF-containing aqueous vanadium electrolyte to improve photocurrent stability (0.35 M V(II) + V(III), 4 M HCl, 0.2 M HF). The photoelectrochemical characteristics of the cell were determined under 75 mW/cm^2 insolation. As shown, under illumination, the AlGaAs|Si|$V^{2+/3+}$ electrolyte photoelectrochemical solar cell exhibits an open-circuit potential V_{oc} = 1.4 V, a short-circuit photocurrent J_{sc} = 12.7 mA/cm^2, and a fill factor FF = 0.81 determined from the fraction of the maximum power P_{max}, compared to the product of the open-circuit potential and short-circuit current.

$$FF = \frac{P_{max}}{V_{oc}J_{sc}} \tag{18}$$

The multiple-bandgap solar-to-electrical conversion efficiency of 19.2% compares favorably with the maximum 15−16% solar-to-electrical energy-conversion efficiency previously reported for single-bandgap photoelectrochemical solar cells.[34] Small photoelectrochemical efficiency losses can be attributed to polarization losses accumulating at the solution interfaces. Under illumination a photocurrent density of 13 mA/cm^2 seen in Figure 7 is consistent with polarization losses of approximately 0.04 V in Figure 6, accumulating both at the anode and at the cathode. At the observed maximum power point photovoltage, in excess of 1.2 V in Figure 7, this combined 0.08-V loss is consistent with an effective loss in efficiency of 0.3−0.4% compared to analogous solid-state photovoltaic cell configurations.

Solar cells with an internal electrochemical component, that is, with ionic and electronic charge transfer, have potential advantages. The ionic charge-transfer-induced in situ chemical oxidation/reduction can be considered for (i) electrochemical-energy storage, (ii) chemical-fuel generation, and (iii) chemical decomposition of pollutants. However a common disadvantage of these systems is photoinduced corrosion of the semiconductor that originates at the semiconductor/solution interface. The corroded surface inhibits charge transfer, which diminishes

photocurrent. An electrocatalyst placed between the semiconductor and the electrolyte can provide a stable solid/solution interface that both facilitates charge transfer and impedes semiconductor photocorrosion. The multiple-bandgap photoelectrochemical cell can utilize this electrocatalyst interface and a bipolar series arrangement of wide- and small-bandgap semiconductors to enhance energy conversion. The photoelectrochemical characterization presented in the inset of Figure 7 summarizes a modified GaAs|Si|V$^{3+/2+}$ MPEC. In this indirect-ohmic photoelectrochemistry, electrolyte-induced photocorrosion of the silicon is entirely inhibited by utilization of an electrocatalyst (a second carbon electrode) bridging charge transfer between the semiconductor and the electrolyte.

Bipolar-gap *indirect-ohmic* photoelectrochemistry comprises either a bipolar-bandgap pnpn|electrolyte ohmic photoelectrochemical cell, with reduction occurring at the semiconductor/electrocatalyst/electrolyte interface and regenerative oxidation occurring at the electrolyte/counter electrode (anode) interface, or an npnp|electrolyte cell with oxidation occurring at the semiconductor/electrocatalyst/electrolyte interface and regenerative reduction occurring at the electrolyte/counter electrode interface. In these systems, *indirect* refers to the catalyst interface that bridges the semiconductor and solution and *ohmic* indicates this interface is an ohmic rather than a Schottky junction. Two highly stable aqueous-phase redox couples, iodide and polysulfide, are used in these studies to further this bipolar indirect multiple-bandgap photoelectrochemistry. The iodide redox couple has been extensively studied in highly stable tungsten or molybdenum chalcogenide (single-bandgap) photoelectrochemical cells,[6–7,35–38] as well as dye-sensitized nanocrystalline TiO$_2$ photoelectrochemical cells.[39] The couple has an aqueous redox potential of 0.5 V versus the standard hydrogen electrode (SHE) expressed as the standard potential for reduction:

$$\tfrac{1}{2}I_3^- + e^- \rightarrow \tfrac{3}{2}I^- \tag{19}$$

The photoelectrochemical solar cells (PECs) utilizing eq 19 contain concentrated iodide electrolytes to improve electrolyte conductivity and mass transfer. In addition to the species inherent to typical aqueous iodide solutions, I$^-$ and I$_3^-$, we have observed that speciation in iodide solutions more concentrated than 1 M contains a significant I$_4^{2-}$ solution-phase component in accord with[40]

$$I^- + I_2 \rightleftarrows I_3^-; \quad K_3 = 720 \tag{20}$$

$$I_3^- + I^- \rightleftarrows I_4^{2-}; \quad K_4 = 0.20 \tag{21}$$
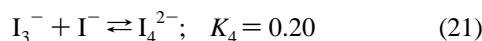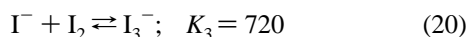
Acidification of iodide solutions can stabilize against decomposition, which occurs in more alkaline solutions, and can occur in accord with[40]

$$3I_2 + 3H_2O \rightleftarrows IO_3^- + 5I^- + 6H^+ \tag{22}$$
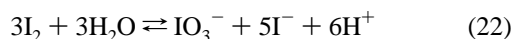
Solution acidification can also facilitate charge transfer. These iodide solution modifications can affect and improve photoelectrochemical energy conversion in tungsten diselenide photoelectrochemical solar cells.[40]

Aqueous polysulfide ($E = -0.5$ V vs SHE) was the earliest redox couple employed in regenerative (single bandgap) photoelectrochemical solar cells.[3–5] Solution-phase modification affects cadmium chalcogenide photoelectrochemistry.[9,41] Charge transfer is limited by the low concentration of supersulfide radical, S$_4^-$, concentration in the electrolytes (S$_4^-$ + e$^-$ $\rightleftarrows$ S$_4^{2-}$)
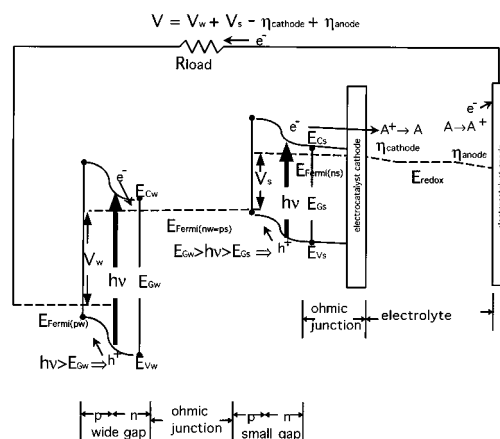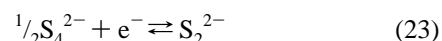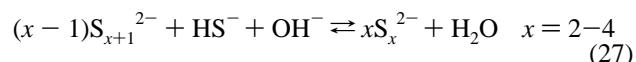

Figure 8. Energy diagram for bipolar *indirect-ohmic* multijunction regenerative photoelectrochemistry. As indicated, an electrocatalyst provides an *indirect-ohmic* contact between the small-bandgap semiconductor and electrolyte.
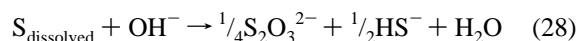
but may be equivalently described by prevalent polysulfide species in solution:[9]

$$\tfrac{1}{2}S_4^{2-} + e^- \rightleftarrows S_2^{2-} \tag{23}$$

The aqueous alkali polysulfide system contains OH$^-$, H$^+$, H$_2$S, HS$^-$, S^{2-}, S$_2^{2-}$, S$_3^{2-}$, S$_4^{2-}$, and S$_5^{2-}$ related by the well-established equilibria equations:[42,43]

$$H_2S \rightleftarrows H^+ + HS^- \tag{24}$$

$$HS^- \rightleftarrows H^+ + S^{2-} \tag{25}$$

$$H_2O \rightleftarrows H^+ + OH^- \tag{26}$$

$$(x-1)S_{x+1}^{2-} + HS^- + OH^- \rightleftarrows xS_x^{2-} + H_2O \quad x = 2-4 \tag{27}$$

In addition to semiconductor decomposition, electrolyte decomposition leads to polysulfide PEC instability.[41,44] Total dissolved sulfur, C_S, decomposes to thiosulfate, S$_2$O$_3^{2-}$, at the measured rate $-dC_S/dt$:

$$S_{dissolved} + OH^- \rightarrow \tfrac{1}{4}S_2O_3^{2-} + \tfrac{1}{2}HS^- + H_2O \tag{28}$$

$$-dC_S/dt = -k_f[S_5^{2-}][OH^-]/[HS^-]; \quad k_f = 10^{-(10.7-5430/T(K))} \tag{29}$$

Polysulfide solutions at room temperature can be stable on the order of years when the concentration of dissolved alkali sulfide salt, C_{M2S}, is kept high relative to the concentration of dissolved sulfur:

$$C_{M2S}/C_S \leq 1 \tag{30}$$

The bipolar-gap indirect-ohmic photoelectrochemical energy diagram in Figure 1 presents electron transfer, under illumination, from the wide- and small-bandgap semiconductor space-charge layers through an electrocatalyst to the solution followed by ionic charge transfer through the bulk electrolyte to the counter electrode, electronic charge transfer through an external load, returning through the semiconductor back contact. In an extension of the direct-ohmic cells of eqs 6 and 7, energy conversion can occur either through Figure 8's photocathodic driven redox process
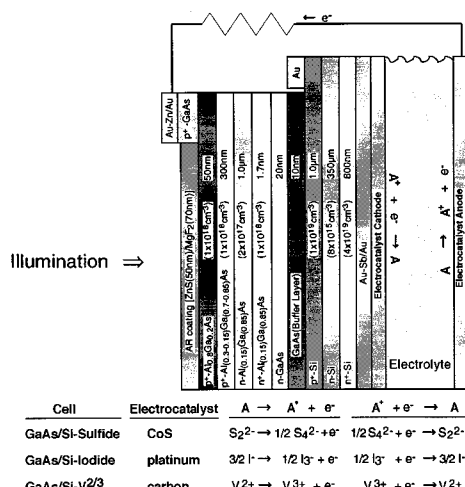
Bipolar Semiconductor Electrochemistry

J. Phys. Chem. B, Vol. 102, No. 14, 1998 **2543**

Figure 9. Schematic description of the components in a bipolar-gap indirect-ohmic AlGaAs|Si|(electrocatalyst)|(redox electrolyte)|(electrocatalyst) photoelectrochemical solar cell. Three experimental systems are described in the text. (1) The electrolyte is $V^{3+/2+}$ ($E° = -0.3$ V vs SHE), and the electrocatalyst cathode and anode are carbon electrodes. (2) The electrolyte is iodide ($E° = 0.5$ V vs SHE), and the electrocatalyst cathode and anode are platinum electrodes. (3) The electrolyte is polysulfide ($E° = -0.5$ V vs SHE), and the electrocatalyst cathode and anode are cobalt sulfide electrodes.

$$hv \Rightarrow pn(\text{wide gap})|pn\ (\text{small gap})|(\text{electrocatalyst})|$$
$$(\text{redox couple})|(\text{electrocatalyst anode}) \quad (31)$$
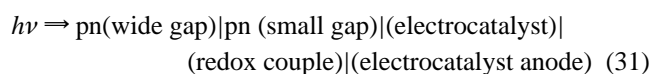
or through a photoanodic driven redox couple

$$hv \Rightarrow np(\text{wide gap})|np\ (\text{small gap})|(\text{electrocatalyst})|$$
$$(\text{redox couple})|(\text{electrocatalyst cathode}) \quad (32)$$
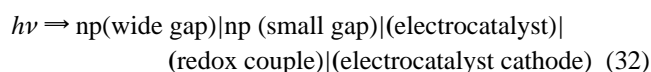
The photocathodic bipolar direct-ohmic MPEC photoelectrochemistry comprises a two-photon/one-electron photoelectrochemical process ($2hv \rightarrow e^-$) injecting charge into an electrocatalyst and then into solution. The bipolar indirect-ohmic MPEC energy diagram of Figure 8 is studied with both a Pt-catalyzed iodide redox couple and a CoS-catalyzed polysulfide redox couple using a tandem AlGaAs ($E_{Gw} = 1.6$ eV) wide bandgap with a Si ($E_{Gs} = 1.0$ eV) small bandgap. The iodide redox couple cell may be summarized through Figure 9. Photogenerated charge at the silicon interface is driven into a Pt electrode via a conductive Au−Sb/Au layer and induces solution-phase I_3^- reduction in accord with eq 19. A counter Pt electrode provides an electrocatalytic anodic surface for the reverse process in a regenerative cell:
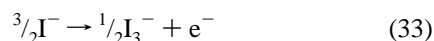
$$^3/_2I^- \rightarrow {}^1/_2I_3^- + e^- \quad (33)$$

Maximization of the photopower necessitates minimization of the anodic and cathodic polarization losses η_{anode} and η_{cathode}. Figure 10 compares the anodic and cathodic polarization curve for charge transfer to the iodide redox couple through either planar platinum or nickel electrodes. In the current domain investigated, iodide anodic and cathodic polarization losses are observed to be highly linear. With only 60% of the polarization losses, the platinum electrode is a more effective electrocatalyst than the nickel electrode for either the cathodic or anodic processes. The Pt polarization of $1.2-1.3$ mV cm^2 /mA can create small but significant losses. For example, at photocurrent densities of approximately 15 mA/cm^2, 15−30 mV of polarization loss will occur in the MPEC.

Figure 11 presents the outdoor characteristics of the iodide

Figure 10. Current density for the $^1/_2I_3^-/^3/_2I^-$ iodide redox couple's oxidation/reduction at either nickel or platinum electrodes (in the dark) for various potentiostatic applied potentials at a linear sweep rate of 5 mV/s.
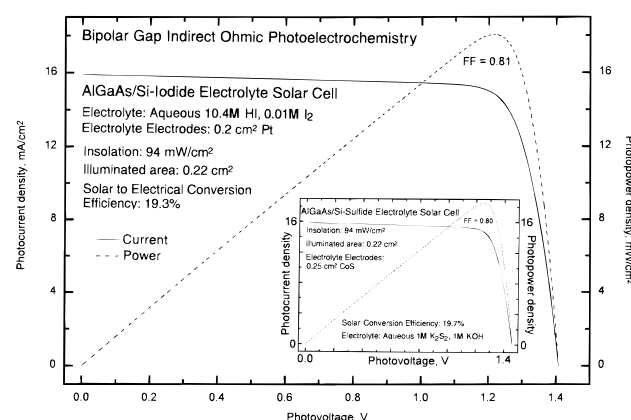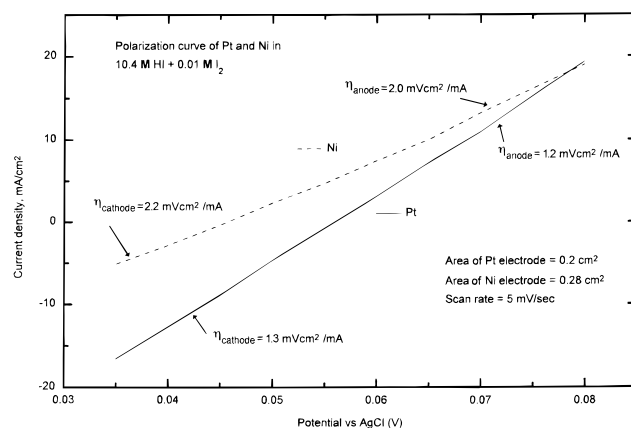

Figure 11. Measured outdoor photocurrent/voltage characteristics of the iodide bipolar-gap indirect-ohmic AlGaAs|Si|Pt|iodide|Pt photoelectrochemical solar cell. Insolation was measured by the Israel Meteorological Society. The insett shows the photocurrent/voltage characteristics of the polysulfide bipolar-gap indirect-ohmic AlGaAs|-Si|CoS|polysulfide|CoS photoelectrochemical solar cell.

bipolar-gap indirect-ohmic AlGaAs|Si|Pt|iodide|Pt photoelectrochemical solar cell under solar illumination. The cell is comprised of the individual constituents illustrated in Figure 9 and uses an aqueous iodide electrolyte containing 10.4 M HI and 0.01 and 4 M I_2. The photoelectrochemical characteristics of the cell were determined under 94 mW/cm^2 insolation. As shown, under illumination, the AlGaAs|Si|Pt|iodide|Pt MPEC exhibits a $V_{oc} = 1.41$ V, $J_{sc} = 15.9$ mA/cm^2, a solar-to-electrical conversion efficiency of 19.3% at $P_{max} = 18.1$ mW/cm^2 and FF = 0.81.

Aqueous polysulfide was the first redox couple employed in (single-bandgap) regenerative photoelectrochemical solar cells. A regenerative polysulfide redox couple multiple-bandgap cell may be summarized through Figure 9. The cell utilizes the same graded band emitter Al$_x$Ga$_{1-x}$As wide-bandgap top layers and Si lower layers as in the iodide bipolar indirect-ohmic MPEC, but the electrocatalytic electrode and electrolyte are respectively replaced by CoS and aqueous polysulfide. Hodes et al. have demonstrated that cobalt sulfide provides an effective electrocatalytic surface for polysulfide oxidation/reduction,[45] and Licht has demonstrated that the CoS electrode is effective in sulfide photoelectrochemical electrolytes[41,46] and electrochemical storage electrolytes for a wide range of current densities.[47−49] We have previously shown that in aqueous alkali polysulfide
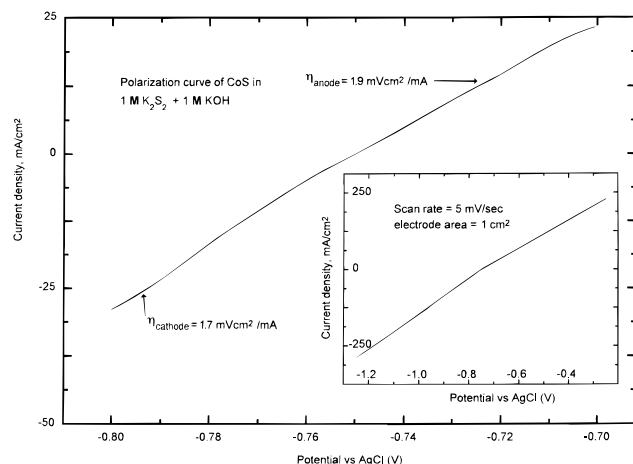
Figure 12. Current density for polysulfide oxidation/reduction (in the dark) at cobalt sulfide electrodes for various potentiostatic applied potentials at a linear sweep rate of 5 mV/s. The inset shows polarization at high current density. The main figure shows polarization at (low) current density comparable to that from solar illumination on MPEC.

electrolytes, polarization losses are significantly less at CoS in potassium compared to sodium or lithium polysulfide electrolytes.[41]
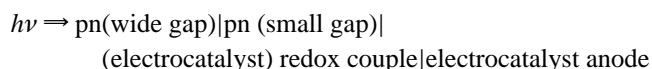
As seen in Figure 12, CoS provides an effective electrocatalytic surface for aqueous potassium polysulfide reduction. Polarization losses are highly linear for anodic and cathodic processes both in the high current density (figure inset) and low current density (main figure) domains. Whereas sulfide adsorption is well-known to "poison" and thereby passivate the Pt surface, this does not occur in the analogous aqueous polyselenide electrolytes, and Pt can be an effective electrocatalyst in the latter media.[46] Compared to CoS, Pt and carbon are poor aqueous sulfur electrocatalysts and exhibit an order of magnitude greater overpotential. At the CoS surface and as seen in Figure 12 at current densities typical of those generated in direct-illumination solar cells, small polarization losses of $1.8(\pm 0.1)$ mV cm^2 mA^{-1} occur at Co in either anodic or cathodic processes in 1 M K$_2$S$_2$ and 1 M KOH. At photocurrent densities in the MPEC of approximately 15 mA/cm^2, 25−50 mV of polarization losses will occur.

The polysulfide bipolar-gap indirect-ohmic AlGaAs|Si|-CoS|polysulfide|CoS photoelectrochemical solar cell, as described in Figure 9, was examined under outdoor insolation. Back-wall illumination prevents any light loss due to solution absorbance, and the CoS/solution interface prevents any semiconductor (Si) decomposition due to electrolyte-induced photocorrosion. Polysulfide reduction occurs at the photodriven CoS cathode in accord with eq 23, as constrained by equilibrium eqs 24−27. Regenerative oxidation occurs at the CoS counteranode. Characteristics were determined under 94 mW/cm^2 insolation and are presented in the inset of Figure 11. The AlGaAs|CoS|polysulfide|CoS MPEC exhibits a V_{oc} = 1.46 V, a short-circuit photocurrent of 15.8 mA/cm^2, a maximum power of 18.5 mW/cm^2, a fill factor of 0.80, and a solar-to0electrical energy conversion efficiency of 19.7%. In subsequent papers, the photoelectrochemistry of other multiple-bandgap systems will be investigated, including those having the potential combined benefits of energy conversion *and* energy storage.

Conclusions

Distinctive multiple-bandgap photoelectrochemistry is possible. In this study, constraints on a bipolar direct multiple-bandgap photoelectrochemistry have been investigated and a

resultant high solar-to-electrical conversion efficiency cell demonstrated. Wide-bandgap pn junctions in tandem monolithic are in contact with smaller bandgap pn junctions. The small-bandgap semiconductor is in ohmic contact with a regenerative solution-phase redox couple in either a photoanodic or a photocathodic manner, with the latter represented as

$$h\nu \Rightarrow \text{pn(wide gap)}|\text{pn (small gap)}|$$
$$\text{(electrocatalyst) redox couple}|\text{electrocatalyst anode}$$

Additional constraints are imposed on multiple-bandgap photoelectrochemical solar cells compared to analogous state systems. These include competition with photon absorption by the solution, solvent electrolysis, and corrosion at the semiconductor electrolyte interface leading to photocurrent instability. It is demonstrated that the energetic photopotentials of such multiple-bandgap systems need not facilitate parasitic solvent decomposition in regenerative photoelectrochemistry and that the solvent electrochemical potential window may be further extended through solution-phase modification. A MPEC in which incident light passes directly into the wide-gap semiconductor layers, rather than through the solution phase, prevents incident photon loss through competitive electrolyte light absorption. Photocurrent instability can be alleviated through solution modification and utilization of an electrocatalyst intermediate.

Multiple-bandgap regenerative photoelectrochemistry can provide efficient conversion of solar-to-electrical energy, generating external electrical work, in which no net change in electrolyte composition occurs. The energy diagram for photocathodic bipolar direct-ohmic regenerative photoelectrochemistry has been evaluated and exemplified with a AlGaAs|Si|V$^{3+/2+}$|carbon photoelectrochemical solar cell. The individual active constituents include a graded band emitter varying from Al$_{(0.3-0.15)}$Ga$_{(0.7-0.85)}$As to improve collection efficiency, a lower smaller-bandgap Si layer in direct contact with an electrolyte, and a carbon anode. The aqueous electrolyte is composed of 0.35 M V(II) + V(III), 4 M HCl, and 0.2 M HF. Addition of HF prevents Si surface passivation and stabilizes the photocurrent. The photoelectrochemical characteristics of the cell were determined outdoors under 75 mW/cm^2 insolation and exhibit an open-circuit potential V_{oc} = 1.4 V, a short-circuit photocurrent J_{sc} = 12.7 mA/cm^2, a fill factor FF = 0.81, and over 19% solar-to-electrical conversion efficiency.

In bipolar semiconductor indirect-ohmic regenerative photoelectrochemistry, the high multiple-bandgap photopotential that may be generated is used to drive a regenerative electrochemical couple via an appropriate (stable, low polarization) electrocatalyst electrode. Examples probed of this bipolar indirect-ohmic multiple-bandgap photoelectrochemical cell include a CoS electrocatalyst, a polysulfide electrolyte, and other Pt electrocatalytic electrodes within an iodide electrolyte. Both examples again utilize a series of AlGaAs wide-bandgap top layers and small-bandgap Si bottom layers. The photoelectrochemical characteristics of the bipolar indirect-ohmic multiple-bandgap cells were determined outdoors under 94 mW/cm^2 insolation, generating in the polysulfide cell a V_{oc} = 1.46 V, J_{sc} = 15.8 mA/cm^2, and FF = 0.80. The characteristics of the iodide cell were V_{oc} = 1.41 V, J_{sc} = 15.9 mA/cm^2, and FF = 0.81. In either cell, the combined polarization losses for cathodic and anodic processes are small (<0.05 V) compared with the maximum power point photopotential of 1.2−1.3 V generated in the cells.

Bipolar Semiconductor Electrochemistry

J. Phys. Chem. B, Vol. 102, No. 14, 1998 **2545**

In both bipolar direct and indirect MPECs investigated, the solar-to-electrical conversion efficiency of 19−20% compares favorably with the maximum 16% solar-to-electrical energy conversion efficiency previously reported for single-bandgap photoelectrochemical solar cells. In related studies we explore fundamental configurations for multiple photoelectrochemistry[50] and specifically those in which the tandem bandgap layers are in an inverted rather than bipolar arrangement.[51] Ongoing studies include multiple-bandgap photoelectrochemistry with in situ energy storage, and multiple-bandgap GaInP$_2$/GaAs photodriven electrochemistry.

References and Notes

(1) Tributsch, H.; Gerischer, H. *Ber. Bunsen-Ges. Phys. Chem.* **1969**, *73*, 850.

(2) Fujishima, A.; Honda, K. *Nature* **1972**, *238*, 37.

(3) Hodes, G.; Manassen, J.; Cahen, D. *Nature* **1976**, *261*, 403.

(4) Ellis, A. B.; Kaiser, S. W.; Wrighton, M. S. *J. Am. Chem. Soc.* **1976**, *98*, 1635.

(5) Miller, B.; Heller, A. *Nature* **1976**, *262*, 680.

(6) Tributsch, H. *Solar Energy Mater.* **1979**, *1*, 257.

(7) Tenne, R.; Wold, A. *Appl. Phys. Lett.* **1985**, *47*, 707.

(8) Licht, S. *Solar Energy Mater. Sol. Cells* **1995**, *38*, 305−319. Licht, S.; et al. *J. Electrochem. Soc.* **1995**, *142*, 1539, 1546. Licht, S.; et al. *J. Phys. Chem.* **1996**, *100*, 9082.

(9) Licht, S. *Nature* **1987**, *330*, 148−151.

(10) Tributsch, H.; Schlichtthorl, G.; Elstner, L. *Electrochim. Acta* **1993**, *38*, 141.

(11) Smith, B. B.; Nozik A. *J. Phys. Chem. B* **1997**, *101*, 2459−2475.

(12) Henry, C. H. *J. Appl. Phys.* **1980**, *51*, 4494.

(13) Friedman, D. J.; Kurtz, S. R.; Bertness, K.; Kibbler, A. E.; Kramer, C.; Olsen, J. M. *Prog. Photovoltaics* **1995**, *3*, 47.

(14) Benner, J. P.; Olson, J. M.; Coutts, T. J. *Advances in Solar Energy*; Boer, K. W., Ed.; American Solar Energy Society, Inc.: New York, 1992; Vol. 7, Chapter 4, p 125.

(15) Green, M. A.; Emery, K.; Bucher, K.; King, D. L.; Sanekazu, Igari. *Prog. Photovoltaics* **1996**, *4*, 321.

(16) Soga, T.; Kato, T.; Yang, M.; Umeno, M.; Jimbo, T. *J. Appl. Phys.* **1995**, *78*, 4196.

(17) Freeouf, J. L.; Woodhall, J. *Appl. Phys. Lett.* **1981**, *39*, 727.

(18) Tersoff, J. *Phys. Rev. Lett.* **1984**, *52*, 465.

(19) Kar, S.; Rajeshwar, K.; Singh, P.; DuBow, J. *Sol. Energy* **1979**, *23*, 129−139.

(20) Nagasubramanian, G.; Wheeler, B. L.; Bard, A. J. *J. Electrochem. Soc.* **1983**, *130*, 1680−1688.

(21) Orazem, M. E.; Newman, J. *J. Electrochem. Soc.* **1984**, *131*, 2569−2589.

(22) Licht, S.; Marcu., V., *J. Electroanal. Interface Electrochem.,* **1986**, *210*, 197−204.

(23) Chandra, S.; Singh, S. L.; Khare, N. *J. Appl. Phys. Lett.* **1986**, *59*, 1570−1577.

(24) Yoneyama, H.; Sakamota, H.; Tamura, H. *J. Phys. Chem.* **1996**, *100*, 1306.

(25) White, J.; Fan, F.-R.; Bard, A. J. *J. Electrochem. Soc.* **1985**, *132*, 544.

(26) Nozik, A. J.; Memming, R. *J. Phys. Chem.* **1996**, *100*, 1306.

(27) Soga, T.; Kato, T.; Umeno, M.; Jimbo, T. *J. Appl. Phys.* **1996**, *79*, 9375.

(28) Shimizu, H.; Egawa, T.; Soga, T.; Jimbo, T.; Umeno, M. *J. Appl. Phys.* **1992**, *31*, L1150.

(29) Yang, M.; Soga, T.; Jimbo, T.; Umeno, M. *J. Appl. Phys.* **1994**, *33*, 6605.

(30) Soga, T.; Yang, M.; Jimbo, T.; Umeno, M. *Jpn. J. Appl. Phys.* **1996**, *35*, 1401.

(31) Licht, S.; Peramunage, D. *J. Electrochem. Soc.* **1993**, *140*, L4−L6.

(32) Memming, R. In *Photochemical Conversion and Storage of Solar Energy*; Pelizzetti, E., Schiavello, M., Eds.; Kluwer Academic: Netherlands, 1991; pp 193−212.

(33) Heller, A.; Lewerenz, H. J.; Miller, B. *J. Am. Chem. Soc.* **1981**, *103*, 200.

(34) Licht, S.; Peramunage, D. *Nature* **1990**, *345*, 330−333.

(35) Tributsch, H. *J. Electrochem. Soc.* **1978**, *125*, 1086.

(36) Parkinson, B. A.; Heller, A.; Miller, B. *Appl. Phys. Lett.* **1978**, *33*, 521.

(37) Schneemeyer, L. F.; Wrighton, M. S. *J. Am. Chem. Soc.* **1979**, *101*, 6496.

(38) Fan, F.-R.; White, H. S.; Bard, A. J. *J. Electrochem. Soc.* **1980**, *127*, 518.

(39) O'Regan, B.; Grätzel, M. *Nature* **1991**, *353*, 737.

(40) Licht, S.; Myung, N. *J. Electrochem. Soc.* **1995**, *142*, 845. Licht, S.; Myung, N.; Tenne, R.; Hodes, G. *J. Electrochem. Soc.* **1995**, *142*, 840. Licht, S.; Myung, N. *J. Electrochem. Soc.* **1995**, *142*, L129.

(41) Licht, S. *J. Phys. Chem.* **1986**, *90*, 1096. Licht, S.; Tenne, R.; Flaisher, H.; Manassen, J. *J. Electrochem. Soc.* **1984**, *131*, 950. Licht, S.; et al. *J. Electrochem. Soc.* **1985**, *132*, 1076; **1986**, *133*, 52, 272, 277.

(42) Licht, S.; Hodes, G.; Manassen, J. *Inorg. Chem.* **1986**, *25*, 2486.

(43) Peramunage, D.; Forouzan, F.; Licht, S. *Anal. Chem.* **1994**, *66*, 378.

(44) Licht, S.; Davis, J. *J. Phys. Chem. B* **1997**, *101*, 2540.

(45) Hodes, G.; Manassen, J.; Cahen, D. *J. Electrochem. Soc.* **1980**, *127,* 544.

(46) Licht, S.; Forouzan, F. *J. Electrochem. Soc.* **1995**, *142,* 1546.

(47) Peramunage, D.; Licht, S. *Science* **1993**, *261*, 1029−1032.

(48) Licht, S.; Hwang, J.; Light, T. S.; Dillon, R. *J. Electrochem. Soc.* **1997**, *144,* 948.

(49) Licht, S.; Jeitler, J.; Hwang, J. *J. Phys. Chem. B* **1997**, *101*, 4959.

(50) Licht, S.; Khaselev, O.; Soga, T.; Umeno, M. *Electrochem. Solid State Lett.*, in press.

(51) Licht, S.; Khaselev, O.; Ramakrishnan, P. A.; Soga, T.; Umeno, M. *J. Phys. Chem. B*, in press.